



MARMARA UNIVERSITY
FACULTY OF ENGINEERING



CFD ANALYSIS OF AIRFLOW CHARACTERIZATION IN INDUSTRIAL PAPER MOLD DRYING OVEN

ALPEREN ARSLAN, OĞUZALP ÇETİN, SEYFETTİN ONUR SARI

GRADUATION PROJECT REPORT
Department of Mechanical Engineering

Supervisor
Prof. Dr. Mehmet Zafer GÜL

ISTANBUL, 2025



**MARMARA UNIVERSITY
FACULTY OF ENGINEERING**



**CFD ANALYSIS OF AIRFLOW CHARACTERIZATION
IN INDUSTRIAL PAPER MOLD DRYING OVEN**

by

Alperen Arslan, Oğuzalp Çetin, Seyfettin Onur Sarı

January, 2025, Istanbul

**SUBMITTED TO THE DEPARTMENT OF MECHANICAL ENGINEERING
IN PARTIAL FULFILLMENT OF THE REQUIREMENTS FOR THE
DEGREE**

OF

BACHELOR OF SCIENCE

AT

MARMARA UNIVERSITY

The author(s) hereby grant(s) to Marmara University permission to reproduce and to distribute publicly paper and electronic copies of this document in whole or in part and declare that the prepared document does not in anyway include copying of previous work on the subject or the use of ideas, concepts, words, or structures regarding the subject without appropriate acknowledgement of the source material.

Signature of Author(s)

Department of Mechanical Engineering

Certified By

Project Supervisor, Department of Mechanical Engineering

Accepted By

Head of the Department of Mechanical Engineering

ACKNOWLEDGEMENT

We would like to express our deepest gratitude to our academic supervisor, Prof. Dr. Mehmet Zafer Güл, for his priceless guidance, support, and encouragement throughout our thesis journey. His expertise and insightful feedback have been instrumental in shaping our work, and we are truly grateful for his patience and dedication.

We also extend our heartfelt thanks to Ömer Karatekin for his generous support, which have greatly assisted us during this process. His help and encouragement have been truly appreciated.

January, 2025

**Alperen Arslan
Oğuzalp Çetin
Seyfettin Onur Sarı**

ABSTRACT

In this study, CFD analysis of industrial drying oven focusing on air flow patterns with respect to varying mass flow rates is presented. The physical geometry of the drying oven used in this study is characterized by a rectangular enclosure with dimensions of 12m x 2m x 2.5m and includes the presence of multiple shelves or trays for product placement. To conduct computational fluid dynamics analysis, Ansys FLUENT software package was utilized, enabling the numerical simulation of the airflow within the drying oven.

Contents

SYMBOLS	v
ABBREVIATIONS.....	vii
LIST OF FIGURES.....	viii
LIST OF TABLES.....	ix
1. INTRODUCTION	1
2. LITERATURE REVIEW	4
3. THEORETICAL BACKGROUND.....	6
3.1. Navier-Stokes Equations.....	8
3.2. RANS Turbulence Models.....	10
3.2.1. Eddy-Viscosity Models (EVM).....	10
3.2.2. Reynolds Stress Model (RSM)	14
4. METHODOLOGY.....	15
4.1. Geometry.....	15
4.2. Meshing Process	17
4.3. Setup and Solutions	19
5. RESULTS.....	23
6. DISCUSSIONS.....	26
6.1. Flow Pattern and Temperature Distribution.....	26
6.2. Velocity Profiles and Implications for Product Integrity	26
7. CONCLUSION.....	27
8. REFERENCES.....	28

SYMBOLS

Re	: Reynolds Number
V	: Flow Speed
\vec{V}	: Velocity Field
U_∞	: Free Stream Velocity
Q	: Volume Flow Rate
\dot{m}	: Mass Flow Rate
t	: Time
ρ	: Density
\vec{g}	: Gravitational Acceleration
ν	: Kinematic Viscosity
ν_t	: Kinematic Turbulent Viscosity
\bar{u}	: Mean Velocity of Fluid Flow
u_t	: Friction Velocity
μ	: Dynamic Viscosity
μ_t	: Turbulent Viscosity
T	: Temperature
p	: Pressure
D_H	: Hydraulic Diameter
A_c	: Cross-Sectional Area
C_f	: Skin Friction Coefficient
f	: Darcy Friction Factor
L	: Characteristic Length
L_T	: Turbulent Length Scale
k	: Turbulent Kinetic Energy
ω	: Turbulent Dissipation Rate
P_ω	: Rate of Production of ω
P_k	: Rate of Production of k
\tilde{P}_k	: Effective Rate of Production of k
h	: Enthalpy
k_{tc}	: Thermal Conductivity
τ_w	: Wall Shear Stress

y_p	: First Cell Height
y^+	: Dimensionless Wall Distance
d	: Shortest Distance to the Nearest Wall
CD_{kw}	: Cross-Diffusion Term
σ_k	: Turbulence Modelling Constant
σ_ω	: Turbulence Modelling Constant
γ	: Turbulence Modelling Constant
β	: Turbulence Modeling Constant
C_μ	: Empirical Constant
λ	: Proportionality Constant
F_1	: Blending Function
F_2	: Blending Function
S	: Strain Rate
S_{ij}	: Mean Rate of Deformation Component
δ	: Unit Tensor
δ_{ij}	: Kronecker Delta Function
τ_{ij}	: Reynold Stress Tensor
G_ϕ	: Turbulence Production
Ω	: Vorticity
$\Gamma_{\phi eff}$: Effective Diffusion Coefficient

ABBREVIATIONS

2D	: Two Dimensional
3D	: Three Dimensional
PDE	: Partial Differential Equation
CFD	: Computational Fluid Dynamics
RANS	: Reynolds-Averaged Navier-Stokes
EVM	: Eddy Viscosity Model
SST	: Shear Stress Transport
DNS	: Direct Numerical Simulation
LES	: Large-Eddy Simulation
RSM	: Reynolds Stress Model
SIMPLE	: Semi Implicit Method for Pressure Linked Equations

LIST OF FIGURES

Figure 1: Main geometry.....	16
Figure 2: Simplified geometry	16
Figure 3: Volume mesh	18
Figure 4: Details of mass flow rates.....	21
Figure 5: Plot of residuals	21
Figure 6: Sum of mass flow rates	22
Figure 7: Contours of velocity	23
Figure 8: Contours of velocity at planes in z-direction	23
Figure 9: Contours of turbulent intensity	24
Figure 10: Contours of temperature	24
Figure 11: Contours of temperature at planes in z-direction.....	25

LIST OF TABLES

Table 1: Details of Local Mesh	17
Table 2: Details of Surface Mesh	17
Table 3: Details of Boundary Layer	18
Table 4: Details of Volume Mesh.....	19
Table 5: Details of Boundary Conditions	20
Table 6: Details of Under Relaxation Factors	20

1. INTRODUCTION

The increasing focus on sustainability and environmental protection has shifted significant attention toward recyclable and bio-based materials as promising alternatives to traditional petroleum-based plastics. These materials derived from renewable resources such as plants, agricultural byproducts and organic waste, have the potential to address multiple environmental challenges. These materials offer a feasible solution to the growing problem of plastic waste and the associated environmental impact. By utilizing renewable resources, they help reduce consumption of finite fossil fuels. In addition to lowering dependence on petroleum, these bio-based materials can also contribute to material recovery, reduction of landfill waste, and the use of renewable resources.

The potential benefits extend beyond just environmental protection; these materials also open new opportunities for developing innovative and high-value products that can further contribute to a more sustainable future, as they enable the creation of advanced applications and the exploration of new markets and industries. Industries are increasingly investing in bio-based materials and technologies to develop more eco-friendly and sustainable product offerings that minimize their environmental impact.

Along with the growing interest in bio-based materials, there has also been a focus on improving the recycling processes for existing materials, including pulp mold, a key component in many paper-based products. Pulp mold, often made from recycled paper fibers, is a highly sustainable material commonly used in packaging, protective inserts, and disposable products such as egg cartons, trays, and food containers. The use of recycled paper fibers in pulp mold not only reduces reliance on virgin materials but also offers an opportunity to divert these materials from landfills, thereby minimizing the associated environmental impact.

Among the various bio-based materials, paper mold stands out as a particularly advantageous alternative to conventional plastics. Unlike many oil-based plastics, which are derived from non-renewable resources and contribute significantly to environmental pollution, paper mold is made from renewable and bio-degradable materials such as recycled paper fibers. This inherent sustainability makes paper mold an attractive option for industries seeking to reduce their environmental footprint.

One of the key advantages of paper mold is its ability to be recycled and reused. While traditional plastics often end up in landfills or the ocean, paper mold can be collected, processed, and reintroduced into the manufacturing cycle, creating a closed-loop system that minimizes waste and improves resource efficiency. Furthermore, paper mold decomposes naturally within weeks to months, in contrast to the hundreds of years required for many plastic materials to break down.

In addition, manufacturing paper molds requires less energy compared to plastic processing, which often involves energy-intensive extraction, refining and polymerization of fossil fuels. Additionally, paper mold products are non-toxic, eliminating the potential health and environmental risks associated with many synthetic chemicals used in plastic production, a critical advantage for food-contact applications.

However, the recycling and production of paper mold are not without challenges. A critical stage in its lifecycle is the drying process, where the molded pulp is dried to achieve the desired shape and moisture content. Industrial drying ovens used for this purpose must balance energy efficiency, temperature uniformity, and drying speed to ensure efficient and consistent recycling of paper mold. Inefficient airflow or uneven temperature distribution can cause uneven drying, leading to issues such as inconsistent product quality, increased energy consumption, and higher greenhouse gas emissions.

The optimization of drying ovens can be supported by analyzing the airflow patterns, temperature distribution and the transport of key parameters within the drying oven. Air distribution can be driven by different forces, for instance, natural wind, mechanical fan, and/or thermal buoyancy. The combination of these flow mechanisms (forced, natural, and mixed convection) creates airflow characteristics with impingement, separation, circulation, reattachment, vortices, buoyancy, etc. With the rapid advance in computer capacity and speed, the computational fluid dynamics (CFD) technique has become a powerful alternative for predicting airflows. CFD is a subbranch of fluid dynamics. In CFD, data structures and numerical analysis are used to solve fluid flow problems. It provides a framework to simulate fluid flow, heat transfer, and associated physical phenomena by solving the governing equations of fluid mechanics and thermodynamics. There are several different CFD solvers available on the market. As computer software of CFD, there are two types of software: One of them is commercial softwares such as Fluent, CFX, StarCD, Polyflow, Flow3D, SCRYU etc. The other

one is open source softwares such as SU2, OpenFOAM. For this analysis Ansys Fluent has been chosen as this is the one available and determined to be sufficient for the analysis.

In this study, CFD is utilized to investigate the performance of a industrial drying oven, focusing on critical parameters such as temperature, velocity, and density distributions of air within the system. Hot air conveyor dryers are widely used in industrial applications due to their efficiency and versatility. These dryers consist of conveyor belts that transport products through a heated air stream. The drying process involves heated air entering the system through an inlet, flowing through perforated plates, and directly contacting the products on the conveyor belts. This interaction facilitates moisture evaporation from the products, driven by heat transfer and mass flow. In this study, the dryer system includes an electric fan powered by a motor to generate hot air. The air enters the drying oven at high temperatures and exits through an outlet maintained at atmospheric pressure. The system operates under specific boundary conditions to ensure uniform drying. By solving the conservation equations of mass, momentum, energy, and species concentrations, CFD can quantitatively calculate various air distribution parameters.

For this study, high-temperature air enters the system at the inlet with a specified mass flow rate and temperature profile. The outlet is maintained at atmospheric pressure to allow free flow of air from the system. All walls of the drying oven and conveyor belts are treated with no-slip conditions, ensuring that the velocity of the fluid at the wall is zero relative to the surface. From these, poly-hexcore mesh was generated for the drying oven. The poly-hexcore mesh combines polyhedral cells in the core region with hexahedral cells near the walls, ensuring a balance between computational efficiency and accuracy. The mesh density was refined near critical regions, such as the perforated plates and the surface of the products, to capture detailed flow and heat transfer phenomena.

When the Reynolds calculation was made with experimental conditions, it was calculated that the flow was in the turbulent region. Generally, CFD predicts turbulent flow through three approaches: direct numerical simulation (DNS), large-eddy simulation (LES), and Reynolds-averaged Navier-Stokes (RANS) equation simulation with turbulence models. DNS computes a turbulent flow by directly solving the highly reliable Navier-Stokes equation without approximations. LES is work on macroscopic structure of turbulent flow. LES provides detailed information on instantaneous airflow and turbulence with the cost of still considerable computing time. For the design and study of air distributions, the mean air parameters are more useful than instantaneous turbulent-flow parameters. Thus, the interest is stronger in solving

the RANS equations with turbulence models that can quickly predict air distributions. Therefore, flow dynamic modelling will be done with Reynolds-Averaged Navier-Stokes's equations. The RANS approach calculates statistically averaged (Reynolds-averaged) variables for both steady-state and dynamic flows and simulates the turbulence fluctuation effect on the mean air flow by using different turbulence models.

The $k-\omega$ SST from RANS models, is a two-equation eddy viscosity model. This model combines the strengths of the $k-\varepsilon$ model for free-stream flows and the $k-\omega$ model for near-wall regions. Since the $k-\omega$ model is too sensitive for free flow modelling, the $k-\omega$ SST model offers a suitable model for all flow. The SST $k-\omega$ model effectively captures flow separation and transition, making it well-suited for simulating air movement through plates with holes and around products in the drying oven. Therefore, the SST $k-\omega$ model was chosen as the turbulence model for this study.

In this study, we aim to extend the existing understanding by conducting a comprehensive CFD analysis of an industrial convectional drying oven under different operating conditions, including a constant tray configuration and a completely empty oven setup. The primary objectives of the CFD analysis are to analyze the air flow, temperature, density etc. distributions within a drying oven, capturing flow dynamics, examine the effects of boundary conditions and mesh generation on simulation accuracy.

2. LITERATURE REVIEW

The performance optimization of industrial drying ovens has been a topic of significant interest in recent years, with researchers employing computational fluid dynamics simulations to gain a deeper understanding of the underlying airflow and heat transfer mechanisms.

Several studies have explored the application of CFD to investigate the dynamic behaviour of various drying processes, including concentration distributions, velocity profiles, and temperature distributions. Sun et al. simulated the velocity and pressure distributions in an industrial dehumidifier wood drying kiln, highlighting the importance of avoiding air recirculation for high efficiency. Similarly, Smit et al. developed a two-dimensional pore-scale model to predict the air flow through a wood drying stack, with favorable comparisons between the simulation results and experimental measurements. Furthermore, Langrish and Keey modelled the air flow patterns in a timber kiln, aiming to predict the distribution of the airflow in the fillet spaces between the boards. [18]

A study by Khatir et al. [19] presented a multi-objective optimization framework for oven designs, utilizing experimentally verified heat transfer correlations and high-fidelity CFD analyses to identify optimal combinations of design features that maximize temperature uniformity and energy efficiency in a bread-baking oven. Another study [18] focused on the industrial drying of wooden pallets, utilizing CFD to analyze the air flow patterns within the drying system. The findings from this study suggested that ensuring uniform and efficient air circulation, without excessive recirculation, was crucial in achieving high performance and energy efficiency in the drying process. The study emphasized the importance of understanding and optimizing the air flow dynamics to improve the overall efficiency and effectiveness of the industrial drying operations for wooden pallets.

Similarly, a CFD based investigation of a rotary bread-baking oven revealed the significant impact of the airflow pattern on the final product quality, emphasizing the potential for numerical simulations to guide the design and operation of such systems. [20] Another study examined the air flow CFD modelling in an industrial convection oven, highlighting the importance of understanding the fluid dynamics within the oven for achieving maximum temperature uniformity and improved product quality. [21]

Researchers have investigated the use of CFD in simulating the complex airflow and drying phenomena in a wide range of industrial drying applications, including can making industry [17], timber kilns [18], and small-scale bread-baking ovens [19]. These studies have shown the usefulness and precision of CFD in providing crucial insights into the complex fluid dynamics and heat transfer in industrial drying systems. This helps guide the design and optimization of such systems by providing valuable insights into the airflow and heat transfer processes, which can ultimately lead to improved energy efficiency and product quality. [17, 18, 19]

In this study, we aim to extend the existing understanding by conducting a comprehensive CFD analysis of an industrial convectional drying oven under different operating conditions, including a constant tray configuration and a completely empty oven setup.

3. THEORETICAL BACKGROUND

The instabilities occurring in the flow cause laminar flow to turn into turbulent flow. Any solid surface projecting towards the flow streamlines is a source of disturbance for the turbulent flow to initiate. If a flow past over a flat plate is investigated, the fully turbulent region does not appear directly after the laminar part. There always appears a transition section which is the region where instabilities in laminar flow start. The flow in this region could be described neither as laminar, nor as turbulent. These instabilities occur due to highly complex fluid-fluid and fluid-solid interactions. If one looks into this phenomenon from partial differential equations point of view, Navier Stokes equations that represent the viscous fluid flow produce instabilities due to the non-linear viscous and inertial terms in these equations. Turbulence is a continuum process. When it comes to a point to measure turbulence elements, length scale appears as a dimensional property. The length scales of eddies which will be explained in the following parts emerges much larger than the molecular length scale. This enables one to treat turbulence as a continuum phenomenon. Then, one can conclude that Navier-Stokes equations have all the physics of turbulence.

A fluid flow could be described in several ways. It could be either compressible or incompressible, viscous or inviscid, in the same manner, either laminar or turbulent. One of the most important parameters is the Reynolds number (Re). For different types of flow (namely, flow in a pipe, flow over a flat plate etc.) different Reynolds numbers of transition from laminar to turbulent flow are defined.

Reynolds number calculated as:

$$Re = \frac{VD_H}{\nu} = \frac{\rho VD_H}{\mu} = \frac{\rho QD_H}{\mu A_c} = \frac{\dot{m}D_H}{\mu A_c} \quad (1)$$

where V is the flow speed, \dot{m} is mass flow rate, Q is volume flow rate, D_H is hydraulic diameter (m), ρ is density, ν is kinematic viscosity, μ is dynamic viscosity, D_H is hydraulic diameter and A_c is cross-sectional area where the fluid enters. When considering pressure loss with respect to the flow in a duct, hydraulic diameter refers to the diameter of the equivalent circular tube. With respect to the flow through a non-circular cross-section, it is the diameter of a circular tube that would have same pressure loss. For rectangular ducts characteristic dimensions, height and width of the cross-sectional area where fluid enters, for internal flow is taken to be formula for the hydraulic diameter.

$$D_H = L = \frac{2ab}{a+b} \quad (2)$$

where L is the characteristic length (m), a and b are height and width of the cross-sectional area respectively, where the fluid enters. Characteristic length is defined to force localization of a stress softening constitutive equation. The length is associated with an integration point. For 2D analysis, it is calculated by taking the square root of the area. For 3D analysis, it is calculated by taking the cubic root of the volume associated to the integration point.

The concept of the boundary layer is fundamental in fluid dynamics and describes the thin layer of fluid adjacent to a solid surface where the effects of viscosity are significant. When a fluid flows over a surface, the interaction between the fluid and the surface creates a velocity gradient. At the surface, the fluid velocity is zero due to the no-slip condition, while further away from the surface, the velocity increases until it matches the free-stream velocity. This region of velocity transition forms the boundary layer. About turbulent boundary layer, the flow becomes chaotic and contains eddies and vortices, leading to higher mixing and energy dissipation.

The thickness of the boundary layer is defined as the distance from the surface where the fluid velocity reaches approximately 99% of the free-stream velocity. The thickness depends on factors such as fluid viscosity, flow velocity, and the distance from the leading edge of the surface. In turbulent boundary layers, the flow near a wall is divided into different regions based on the dominance of viscous and turbulent effects. These regions are essential in characterizing the velocity profile and behaviour of the boundary layer.

The three primary regions are viscous sublayer, buffer layer and logarithmic layer. This classification is made according to the y^+ value. y^+ is a dimensionless parameter that quantifies the distance from the wall in viscous sublayer units. Viscous sublayer is closest to the wall, extending up to $y^+ = 5$. Viscous forces dominate in this layer, and turbulence effects are negligible and provide a baseline for accurately predicting shear stress and drag at the wall. Buffer layer extends from $y^+ = 5$ to $y^+ = 30$. Buffer layer is the transitional region that both viscous and turbulent effects are significant. The behaviour of the fluid in this layer is complex and influenced by both wall shear and turbulence. Logarithmic layer is where $y^+ > 30$ turbulent effects dominate in this region, with viscosity playing a negligible role.

First layer thickness is calculated as:

$$y_p = y^+ + \frac{\mu}{\rho \times u_t} \quad (3)$$

$$u_t = \sqrt{\frac{\tau_w}{\rho}} = \sqrt{\frac{f}{8}} \times U_\infty \quad (4)$$

$$\tau_w = C_f \times \frac{1}{2} \rho U_\infty^2 = \frac{f}{4} \times \frac{1}{2} \rho U_\infty^2 \quad (5)$$

$$4C_f = f = \frac{1}{(1.82 \times \log_{10}(Re) - 1.64)^2} = \frac{1}{(0.79 \times \ln(Re) - 1.64)^2} \quad (6)$$

where u_t is friction velocity, τ_w is wall shear stress, C_f is skin friction coefficient, f is Darcy friction factor, U_∞ is free stream velocity (mean velocity).

3.1. Navier-Stokes Equations

Navier-Stokes equations are equations that describe the three-dimensional motion of viscous fluid substances. Flow field is characterized by balance in mass, momentum, and total energy described by the continuity equation, the momentum equation, and the energy equation. The conservation of mass is based on the continuity equation, conservation of momentum is based on Newton's second law of motion principle, and the conservation of energy equation is based on the first law of thermodynamics principle. Thus, applying the fundamental laws of mechanics to a fluid gives governing partial differential equations for a fluid.

The continuity equation, the momentum equation, and the total energy equations for incompressible fluids are shown below respectively.

$$\frac{\partial \rho}{\partial t} + \nabla \cdot (\rho \vec{V}) = 0 \quad (7)$$

$$\rho \frac{\partial \vec{V}}{\partial t} + \rho \vec{V} \cdot (\nabla \cdot \vec{V}) = -\nabla p + \nabla \cdot \tau_{ij} + F \quad (8)$$

$$\frac{\partial}{\partial t} (\rho h) + \nabla \cdot (\rho \vec{V} h) = \nabla (k_{tc} \nabla T) + \nabla (-p \vec{V} + \tau_{ij} \vec{V}) + F \vec{V} \quad (9)$$

Solutions of the above equations gives velocity field \vec{V} , pressure p , and temperature T , of the fluid in the specified region. Term ρ is density, F is the external forces (gravitational forces, magnetic forces, etc.), t is time, \vec{g} is the gravitational acceleration, k_{tc} is the thermal conductivity, h is the enthalpy.

τ_{ij} is the viscous stress tensor.

$$\nabla \cdot \tau_{ij} = \mu \nabla^2 \vec{V} \quad (10)$$

According to the general deformation law of Newtonian viscous fluid given by Navier-Stokes equation, τ_{ij} is expressed as:

$$\tau_{ij} = -p\delta + \mu \left(\frac{\partial u_i}{\partial x_j} + \frac{\partial u_j}{\partial x_i} \right) + \delta \lambda \nabla \vec{V} \quad (11)$$

where δ is the unit tensor and λ is the proportionality constant. For steady state situation, variables related to time and time variable are dropped from above equations to get simplest form of conservation of mass (continuity equation) and momentum equations. Thus, Navier-Stokes equations for continuity and momentum are:

$$\nabla \cdot \vec{V} = 0 \quad (12)$$

$$\rho \vec{V} (\vec{V} \cdot \nabla) = -\nabla p + \mu \nabla^2 \vec{V} + F \quad (13)$$

For compressible fluids the continuity equation, the momentum equation, and the total energy equations are shown below respectively.

$$\frac{\partial \rho}{\partial t} + \nabla \cdot (\rho \vec{V}) = 0 \quad (14)$$

$$\rho \frac{\partial \vec{V}}{\partial t} + \rho \vec{V} (\nabla \cdot \vec{V}) = -\nabla p + \nabla \left[\mu \left(\nabla \cdot \vec{V} + (\nabla \cdot \vec{V})^T - \frac{2}{3} (\nabla \cdot \vec{V}) I \right) \right] + F \quad (15)$$

$$\frac{\partial E}{\partial t} + \nabla \left[(E + p) \vec{V} - \mu \left(\nabla \cdot \vec{V}^T + (\nabla \cdot \vec{V}^T)^T - \frac{2}{3} (\nabla \cdot \vec{V}) I \right) \vec{V} - k_{tc} \nabla T \right] = F \cdot \vec{V} \quad (16)$$

Term I is the unit tensor. E is the total energy per unit volume described as:

$$E = \rho \left(e + \frac{1}{2} \vec{V}^2 \right) \quad (17)$$

where term $e + \frac{1}{2} \vec{V}^2$ is the enthalpy and e is the internal specific energy of fluid. For steady state situation Navier-Stokes equations becomes:

$$\nabla \cdot \vec{V} = 0 \quad (18)$$

$$\rho \vec{V} (\nabla \cdot \vec{V}) = -\nabla p + \nabla \left[\mu \left(\nabla \cdot \vec{V} + (\nabla \cdot \vec{V})^T - \frac{2}{3} (\nabla \cdot \vec{V}) I \right) \right] + F \quad (19)$$

These equations along with the conservation of energy equation form a set of coupled, nonlinear partial differential equations. It is not possible to solve these equations analytically for most engineering problems. However, it is possible to obtain approximate computer-based

solutions to the governing equations for a variety of engineering problems. This is the subject matter of Computational Fluid Dynamics (CFD).

The equations governing a turbulent flow are precisely the same as for a laminar flow; however, the solution is clearly much more complicated in this regime. The approaches to solving the flow equations for a turbulent flow field can be roughly divided into two classes. Direct numerical simulations (DNS) use the speed of modern computers to numerically integrate the Navier Stokes equations, resolving all of the spatial and temporal fluctuations, without resorting to modeling. In essence, the solution procedure is the same as for laminar flow, except the numerics must contend with resolving all of the fluctuations in the velocity and pressure. DNS remains limited to very simple geometries (e.g., channel flows, jets and boundary layers) and is extremely expensive to run. The alternative to DNS found in most CFD packages (including FLUENT) is to solve the Reynolds Averaged Navier Stokes (RANS) equations. RANS equations govern the mean velocity and pressure. Because these quantities vary smoothly in space and time, they are much easier to solve. They require modeling to “close” the equations and these models introduce significant error into the calculation. Compared with traditional methods such as field measurements and wind tunnel tests, the CFD numerical simulation method has many advantages, including easy modeling, convenient control, and the changing and repeating of the test conditions, as well as being able to give quantitative results.

3.2. RANS Turbulence Models

RANS turbulence models are divided into two primary categories: eddy-viscosity models and Reynolds-stress models.

3.2.1. Eddy-Viscosity Models (EVM)

Eddy-viscosity models are classified according to the number of transport equations used.

a) Zero-Equation Eddy-Viscosity Model

The zero-equation turbulence models are the simplest eddy-viscosity models. The models have one algebra equation for turbulent viscosity and no additional partial differential transport equations (PDE) beyond the Reynolds-averaged equations for mass, momentum, energy, and species conservation. Prandtl (1925) had developed the first known zero-equation model with the mixing-length hypothesis. Theoretically mixing-length model is not a complete one thus calibration must be conducted for each specific type of flow is essential. It can provide satisfactory results for prediction of simple turbulent flow problems with low Reynolds

numbers. The turbulent viscosity correlations of zero-equation models may sometimes fail due to the inherent physical deficiencies, such as not considering non-local and flow-history effects on turbulent eddy viscosity. With lots of obstacles in flow field make this model unreliable.

b) One-Equation Eddy-Viscosity Model

One-equation turbulence models use additional turbulence variables (such as the turbulent kinetic energy, k) to calculate eddy viscosity.

$$\nu_t = C \frac{L_T}{k^2} \quad (20)$$

Where on resolving transport equation kinetic energy (k) is obtained, turbulence length scale is denoted by L_T , and C denotes constant of coefficient. Similar to zero equation turbulent model it is required to set length scale for turbulent in this model.

c) Two-Equations Eddy-Velocity Models

In addition to the k -equation, two-equation eddy-viscosity models solve a second partial differential transport equation to represent more turbulence physics. Two-equation models are generally superior to zero- and one-equation models because they do not need prior knowledge of turbulence structure. Two equations eddy viscosity models can characterize more turbulent mechanisms and provide better visualization for flow. In the two equations models two variables are considered for solution of flow problem. Here the first transportation variable is ' k ' turbulent kinetic energy, and second variable " ε " signify the rate of dissipation of kinetic energy. These models perform well for fluid flow around complex geometries, in open channels, enclose environment with uniform geometry conditions. In two-equation eddy-viscosity turbulence modeling k - ε and k - ω models with two equations are usually used. k - ε model family is popular turbulence model and has the largest number of variants.

The turbulent eddy viscosity, ν_t , is calculated in the k - ε model as follows:

$$\nu_t = C_\mu \frac{k^2}{\varepsilon} \quad (21)$$

where C_μ is an empirical constant. In the k - ω models, ω is the ratio of ε over k . Compared to the k - ε models are superior in predicting equilibrium adverse pressure flows while less robust in wake region and free-shear flows. This led to the development of an integrated model that takes advantage of both models, a successful model named Shear Stress Transport (SST) model developed by Menter (1994). The SST model is essentially a model near wall boundaries and is equivalent to a transformed model in regions far from walls. The switch between them and

formulations is controlled by blending functions. Most eddy viscosity models assume isotropic turbulence structures, which could fail for flows with strong anisotropic behaviors, such as swirling flows and flows with strong curvatures. Menter's $k - \omega$ shear stress transport (SST) model comprises two equations. One for k , the specific turbulent kinetic energy:

$$\frac{\partial}{\partial t}(\rho k) + \frac{\partial}{\partial x_i}(U_i \rho k) = \frac{\partial}{\partial x_j} \left(\mu_k \frac{\partial}{\partial x_j} k \right) + \tilde{P}_k - \beta^* \rho \omega k \quad (22)$$

Another for ω , the specific turbulent dissipation rate (or specific turbulent frequency):

$$\frac{\partial}{\partial t}(\rho \omega) + \frac{\partial}{\partial x_i}(U_i \rho \omega) = \frac{\partial}{\partial x_j} \left(\mu_\omega \frac{\partial}{\partial x_j} \omega \right) + P_\omega - \beta \rho \omega^2 + 2\rho(1 - F_1) \frac{1}{\omega} \frac{1}{\sigma_{\omega,2}} \frac{\partial}{\partial x_j} k \frac{\partial}{\partial x_j} \omega \quad (23)$$

The two terms on the left side of the equations are related to the rate of change of k or ω and the transport of k or ω by convection, respectively. The three terms in common on the right side of equations represent the transport of k or ω by turbulent diffusion, the rate of production of k or ω and the rate of dissipation of k or ω , in this order. The effective viscosities are:

$$\mu_k = \mu + \mu_t \frac{1}{\sigma_k} \quad \mu_\omega = \mu + \mu_t \frac{1}{\sigma_\omega} \quad (24)$$

where μ_t is the modified eddy (or turbulent) viscosity and σ_x ($x = k; \omega$) are diffusion constants of the model. The Reynolds stresses τ_{ij} are computed as usual in two-equation models with the Boussinesq expression:

$$\tau_{ij} = -\rho \overline{U'_i U'_j} = 2\mu_t S_{ij} - \frac{2}{3} \rho k \delta_{ij} \quad (25)$$

S_{ij} represents the mean rate of deformation component and δ_{ij} is the Kronecker delta function. P_ω , the rate of production of ω is given by:

$$P_\omega = \gamma \left[2\rho S_{ij} \cdot S_{ij} - \frac{2}{3} \rho \omega \left(\frac{\partial}{\partial x_j} U_i \right) \delta_{ij} \right] \quad (26)$$

where γ is a model constant.

The SST turbulence closure of Menter (1994), Menter, Kuntz, and Langtry (2003) contains two blending functions, F_1 and F_2 , which bridge the near-wall $k - \omega$ formulation with the away-from-wall $k - \varepsilon$ formulation (expressed in terms of k and ω). These blending functions involve explicit measure of wall distance. In this formulation, the blending function of the model coefficients (F_1) is equal to one in the inner part of the boundary layer to

have Wilcox's $k - \omega$ model near solid walls, while in the outer part, near boundary layer edges and in free-shear layers. blending function F_1 as defined by:

$$F_1 = \tanh \left(\left[\min \left\{ \max \left\{ \frac{L_t}{d}; \frac{500v_t}{d^2\omega} \right\}, \frac{4\rho\sigma_{\omega,2}k}{CD_{kw}d^2} \right\} \right]^4 \right) \quad (27)$$

Where CD_{kw} stands for the positive portion of the cross-diffusion in the $k - \omega$ model. F_1 is limited (varies) from unity at the wall to zero outside wall boundary layers. The first argument in Eq. (27), $L_t \left[= \frac{\sqrt{k}}{(0.09\omega)} \right]$, represents the turbulent length scale, divided by d , the shortest distance to the nearest wall.

The positive portion of CD_{kw} , the cross-diffusion term, is limited as:

$$CD_{kw} = \max \left(2\rho \frac{1}{\omega} \frac{1}{\sigma_{\omega,2}} \frac{\partial}{\partial x_i} k \frac{\partial}{\partial x_i} \omega; 10^{-1} \right) \quad (28)$$

Each coefficient of the Menter's model ($\varphi \equiv \sigma_k, \sigma_\omega, \beta, \gamma$) is evaluated from Eq. (15):

$$\varphi = \varphi_1 F_1 + \varphi_2 (1 - F_1) \quad (29)$$

where the subscript 1 in (φ) is related to the adjusted $k - \omega$ model and the subscript 2 relates to the standard $k - \omega$ model,

The constants values for φ are given as follows:

$$\sigma_{k,1} = 1.176 \quad \sigma_{k,2} = 1.0$$

$$\sigma_{\omega,1} = 2 \quad \sigma_{\omega,2} = 1.168$$

$$\beta_1 = 0.075, \quad \beta_2 = 0.0828, \quad \beta^* = 0.09, \quad K = 0.41,$$

$$\gamma_1 = \left(\frac{\beta_1}{\beta^*} \right) - \left(\frac{\sigma_{\omega,1} K^2}{(\beta^*)^{\frac{1}{2}}} \right) = 0.5532$$

$$\gamma_2 = \left(\frac{\beta_2}{\beta^*} \right) - \left(\frac{\sigma_{\omega,2} K^2}{(\beta^*)^{\frac{1}{2}}} \right) = 0.44$$

Adverse pressure gradients and wake regions are obtained by limiting the eddy viscosity:

$$v_t = \frac{\mu_t}{\rho} = \frac{a_1 k}{\max(a_1 \omega, SF_2)} \quad (30)$$

given that $S = \sqrt{(2S_{ij}S_{ij})}$ is the invariant measure of the strain rate, $\alpha_1 (= 0.31)$ is a constant, v_t is the kinematic eddy viscosity. In turbulent boundary layers, the maximum value of the eddy viscosity is limited by forcing the turbulent shear stress to be bounded. This effect is achieved with the absolute value of the vorticity Ω and the blending function F_2 , defined as a function of wall distance d :

$$F_2 = \tanh \left(\left[\max \left(2 \frac{L_t}{d}; \frac{500\mu}{\rho d^2 \omega} \right) \right]^2 \right) \quad (31)$$

For other regions of the boundary layer, the eddy viscosity can be evaluated as:

$$\mu_t = \rho \left(\frac{k}{\omega} \right) \quad (32)$$

For the $k-\omega$ SST model proposed by Menter this definition of the turbulent eddy viscosity is modified by using a blending function F_2 which is active in boundary layer flows,

$$v_t = \frac{\mu_t}{\rho} = \frac{k/\omega}{\max \{ 1, \Omega F_2 / (\alpha_1 w) \}} \quad (33)$$

To prevent the build-up of turbulence in stagnation regions, \tilde{P}_k , the effective rate of production is limited as follows:

$$\tilde{P}_k = \min(P_k; 10\beta^* \rho k \omega) \quad (34)$$

Where P_k , the rate of production is expressed by:

$$P_k = 2\mu_t S_{ij} \cdot S_{ij} - \frac{2}{3} \rho k \left(\frac{\partial}{\partial x_j} U_i \right) \delta_{ij} \quad (35)$$

3.2.2. Reynolds Stress Model (RSM)

Most eddy viscosity models assume isotropic turbulence structures, which could fail for flows with strong anisotropic behaviours, such as swirling flows and flows with strong curvatures. Reynolds Stress Model (RSM) explicitly solves the transport equations of Reynolds stress and fluxes instead of eddy viscosity. As a result, RSM enable to better handle the anisotropic condition than other RANS eddy viscosity model. Many higher order turbulence correlations remain unexplained during the derivation of Reynolds stresses transportation equations for RSM. However, the derivation of the Reynolds stresses transport equations leads to higher-order unsolved turbulence correlations which need be modelled to close the equations. It provides slightly better results than $k-\epsilon$ model but takes higher computing capacity and time.

All turbulence models mentioned above can be written in a general form as follows:

$$\rho \frac{\partial \bar{\phi}}{\partial t} + \rho \phi \frac{\partial \bar{\phi}}{\partial x_j} - \frac{\partial}{\partial x_j} \left(\Gamma_{\phi, eff} \frac{\partial \bar{\phi}}{\partial x_j} \right) = S_\phi \quad (36)$$

where ϕ represents variables, $\Gamma_{\phi, eff}$ represents the effective diffusion coefficient and S_ϕ represents the source term of an equation.

For SST $k-\omega$ turbulence model:

ϕ	$\Gamma_{\phi, eff}$	S_ϕ	Constants and Coefficients
k ,	$\mu + \mu_t/\sigma_k$,	$\tilde{G}_k - Y_k$	$\mu_t = \frac{\rho k}{\omega} \frac{1}{\max[1/\alpha^*, SF_2/a_1\omega]}; \tilde{G}_k = \min(G_k, 10\rho\beta^* k\omega); G_\omega = \frac{\rho\alpha G_k}{\mu_t};$
ω	$\mu + \mu_t/\sigma_\omega$	$G_\omega - Y_\omega + D_\omega$	$Y_k = \rho\beta^* k\omega; Y_\omega = \rho\beta\omega^2; D_\omega = 2(1-F_1)\rho\sigma_\omega^2 \frac{1}{\omega} \frac{\partial k}{\partial x_j} \frac{\partial \omega}{\partial x_j}; \alpha^* = \frac{\beta_i/3 + (\text{Re}_t/6)}{1 + (\text{Re}_t/6)}; \text{Re}_t = \frac{\rho k}{\mu\omega}; \beta^* = \beta_\infty \frac{4/15 + (\text{Re}_t/8)^4}{1(\text{Re}_t + 8)^4}$

Where, u_i is the velocity component in i direction, T is the air temperature, k is the kinetic energy of turbulence, ε is the dissipation rate of turbulent kinetic energy, ω is the specific dissipation rate of turbulent kinetic energy, p is the air pressure, μ_t is the eddy viscosity, G_ϕ is the turbulence production for ϕ , and S is the rate of the strain.

4. METHODOLOGY

4.1. Geometry

Since the internal flow in the drying oven is being modelled, all elements outside the main geometry of the oven (e.g., electric motor, fan) were removed. Inside the geometry, elements that could affect the flow, such as chains, indentations and protrusions on trays and oven walls, were cleaned. Unnecessary details on the outer walls of the drying oven were also eliminated. Both the inner and outer walls were designed so that each face consisted of a single surface.

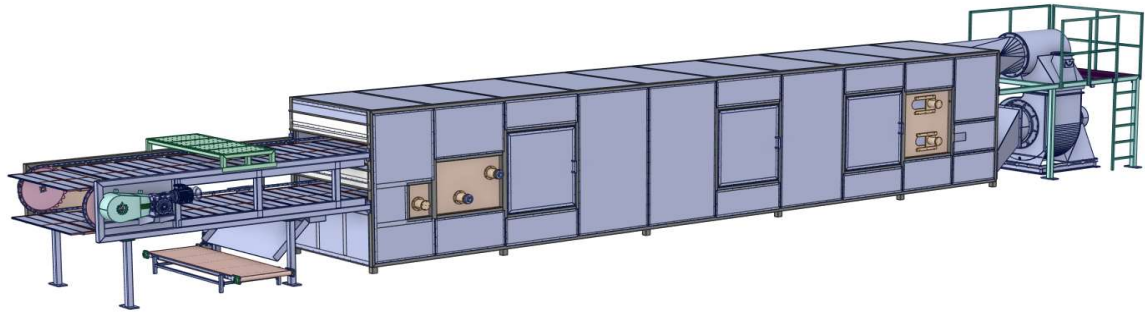


Figure 1: Main geometry

Inside the drying oven, we designed belts positioned according to the entry & exit sections and the motion cycle of the paper pulps within the oven. These belts carry the paper pulps and enable their movement within the oven. Small-diameter channels were designed at the section where hot air enters to allow contact with the paper pulps on the belts. These channels will ensure the passage of hot air coming from the inlet section towards paper pulps. Another channel set with the same diameter as the inlet channels was created to direct the circulating air inside the oven to the outlet section.

Thus, the geometry was designed according to the hot air enters from inlet section and flow through the channels, mixing with the air entering from the sections where the paper pulp enters and exits, and moves on toward the outlet section by the passing from exit channels.

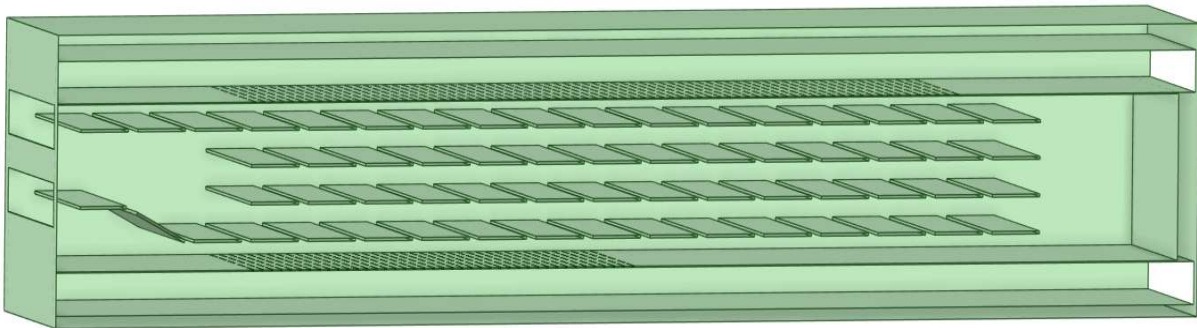


Figure 2: Simplified geometry

Since the air flows within the volume of the geometry, the volume was created using SpaceClaim. In this volume, the section where the air enters was labelled as "inlet," the section where the air exits was labelled as "outlet," and the sections where paper pulps enter and exit were labelled as "exit." The belts carrying the paper pulps were labelled as "tray," the small-diameter channels for air passage were labelled as "holes," and all remaining surfaces were labelled as "wall."

4.2. Meshing Process

4.2.1. Local Mesh

Small circular channels have high curvature and limited space. Local face sizing was applied to small circular channels. Air passes through these small channels before reaching the trays. A fine mesh in these areas ensures that velocity and temperature gradients and flow patterns are accurately captured. Since air interacts with the channel walls, a finer mesh helps in accurately resolving the boundary layer effects.

Table 1: Details of Local Mesh

	Inlet & Outlet	Openings	Holes	Inside Surfaces
Target Mesh Size (m)	0.035	0.035	0.03	0.035

4.2.2. Surface Mesh

For surface mesh, curvature and proximity were used together. Curvature refinement ensures smooth, high-quality elements on circular channels for accurate airflow modelling. Proximity refinement ensures adequate resolution between trays, so the CFD solver correctly captures airflow patterns and heat transfer.

Table 2: Details of Surface Mesh

Minimum Size (m)	Maximum Size (m)	Growth Rate	Curvature Normal Angle (deg)
0.0125	0.04	1.2	18

4.2.3. Boundary layer

When a fluid flows over a surface, the interaction between the fluid and the surface creates a velocity gradient. At the surface, the fluid velocity is zero due to the no-slip condition. The region of velocity transition forms the boundary layer.

The first layer thickness calculation was made according to the $y+$ value taken as 5. First layer thickness determines the first cell size while at the same time providing increasing cell sizes starting from the first cell for the boundary layer. This increase provides a smooth transition with the volume mesh at the end of the boundary layer. This ensured that mesh resolution captures the flow characteristics within the **viscous sublayer**, where the velocity profile is predominantly affected by viscous effects. This approach is necessary for accurately resolving near-wall treatments.

Table 3: Details of Boundary Layer

Number of Layers	Growth Rate	First Height (m)	Offset Method
5	1.2	0.0025	Uniform

4.2.4. Volume Mesh

For volume meshing poly-hexcore elements are applied. Poly-hexcore mesh is a hybrid meshing approach combining polyhedral cells near walls and hexahedral core cells in the bulk region. Thus, polyhedral layers improve the resolution of near-wall effects and hexahedral core reduces the number of cells while maintaining accuracy. So, better display of boundary layers was achieved in the drying oven. These are the reasons for applying poly-hexcore mesh.

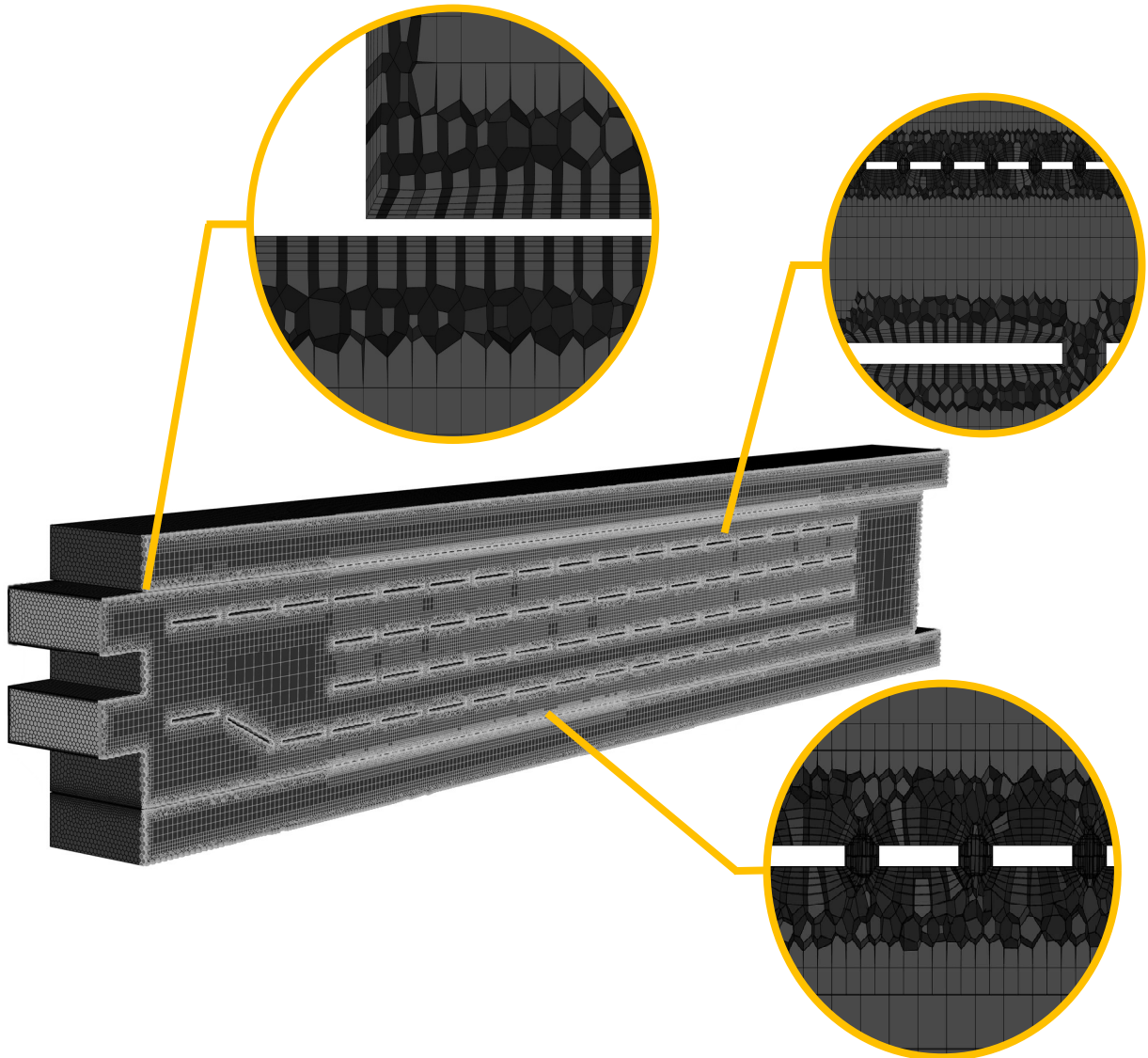


Figure 3: Volume mesh

Table 4: Details of Volume Mesh

Element Type	Minimum Cell Length (m)	Maximum Cell Length (m)	Total Cell Count
Poly-hexcore	0.0126	0.2016	6,820,704

4.3. Setup and Solutions

Since time-dependent analysis are not performed, in the Fluent setup, we selected the solver as steady. Energy model was activated because temperature-dependent analyses were performed. For the turbulence model, the SST k-omega viscous model was selected and the model constants were kept at their default values. For the material section, aluminum was selected for the solid, and air for the fluid. The temperature-dependent properties of air which are density, specific heat, thermal conductivity, and viscosity, were defined using a piecewise-linear approach, and their graphs were plotted. This ensured that the thermal properties of air at any given temperature would be automatically selected. For boundary conditions:

- The inlet was defined as the mass flow inlet and the mass flow rate is defined as 3.5 kg/s, 4.2 kg/s and 5 kg/s for three different simulations depending on the fan which is pushing the hot air. The inlet temperature was set to 180°C for all simulations.
- The outlet was defined as a pressure outlet. Since there is no pressure variation, it was assumed to be atmospheric pressure, and the gauge pressure was defined as 0. The temperature needed to be defined slightly above room temperature because convection heat transfer from the high temperature of the drying oven increases the ambient temperature slightly. Therefore, the temperature was defined as 30°C.
- Since the fan, located outside the outlet section, draws air from inside the oven, the exit sections were defined as velocity inlets. The air inlet velocity was defined as 1.5 m/s, and the temperature was defined as 30°C.
- The walls of the drying oven were defined as stationary with a no-slip shear condition.

Table 5: Details of Boundary Conditions

Boundary Conditions					
Section	Type	Conditions			Temperature
Inlet	Mass Flow Inlet	3.5 kg/s	4.2 kg/s	5.0 kg/s	180 °C
Outlet	Pressure Outlet	1 atm			30 °C
Opening	Velocity Inlet	1.5 m/s			30 °C
Wall	Stationary Wall	No slip			~

To enforce mass conservation, reduce discontinuity and oscillation in the prediction of momentum, turbulent kinetic energy and specific dissipation rate, SIMPLE algorithm was used for solution method scheme. Also warped face gradients correction was disabled because this is recommended for polyhedral cases. The remains are default. We decreased the viscosity, momentum, specific dissipation rate and turbulent kinetic energy values to continue the decrease of the residuals and to converge criteria. We also decreased the density and energy values since the density changes depending on the temperature. Thus, the desired convergence was achieved.

Table 6: Details of Under Relaxation Factors

Under-Relaxation Factors	
Pressure	0.3
Density	0.8
Body Forces	1
Momentum	0.4
Turbulent Kinetic Energy	0.6
Specific Dissipation Rate	0.6
Turbulent Viscosity	0.8
Energy	0.6

In addition to the residuals, mass flow rate graph was added to the monitor to check whether the total mass flow rate from the inlet section to the outlet section converges to zero.

Mass Flow Rate	[kg/s]
openings	2.3564446
inlet	4.9999976
outlet	-7.3566527
Net	-0.00021040245

Figure 4: Details of mass flow rates

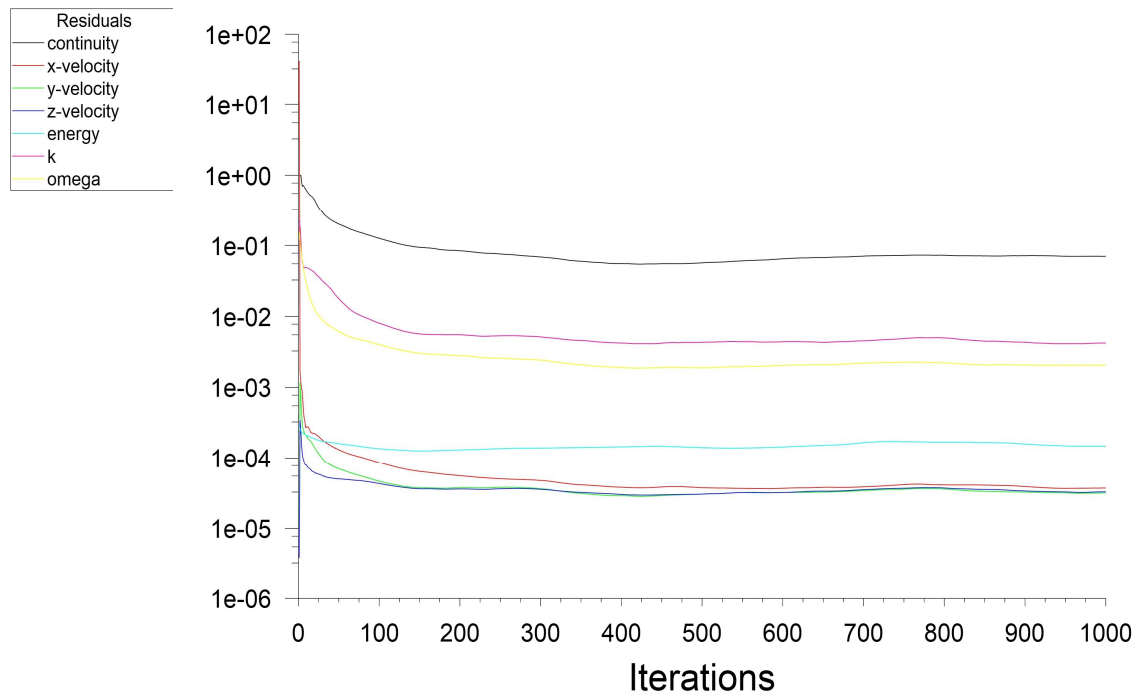


Figure 5: Plot of residuals

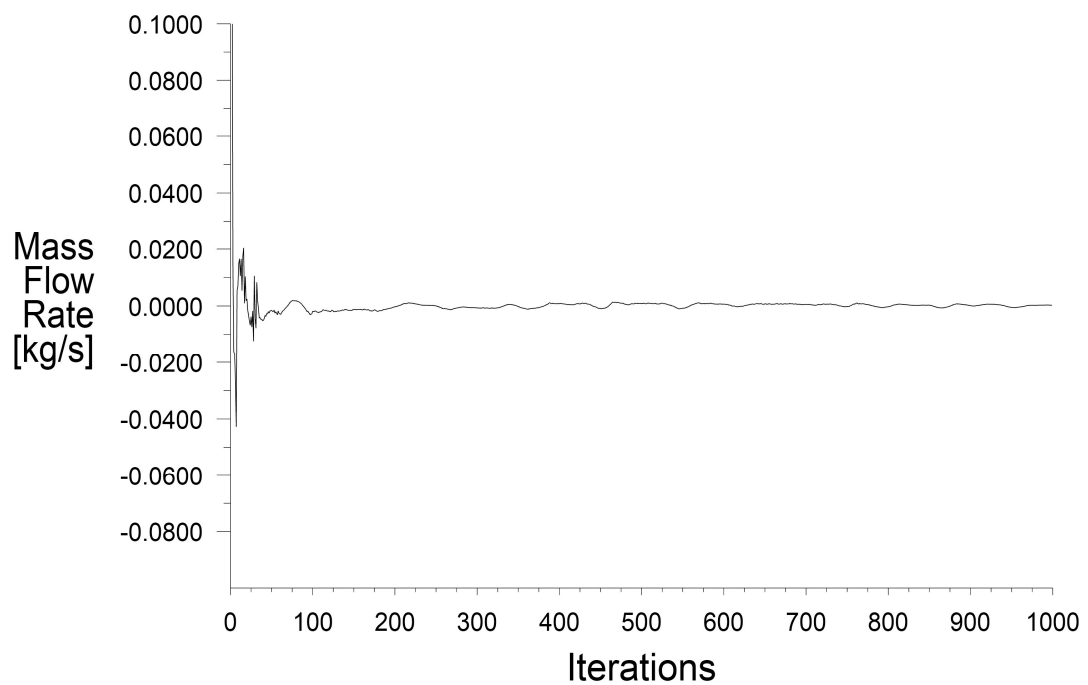


Figure 6: Sum of mass flow rates

5. RESULTS

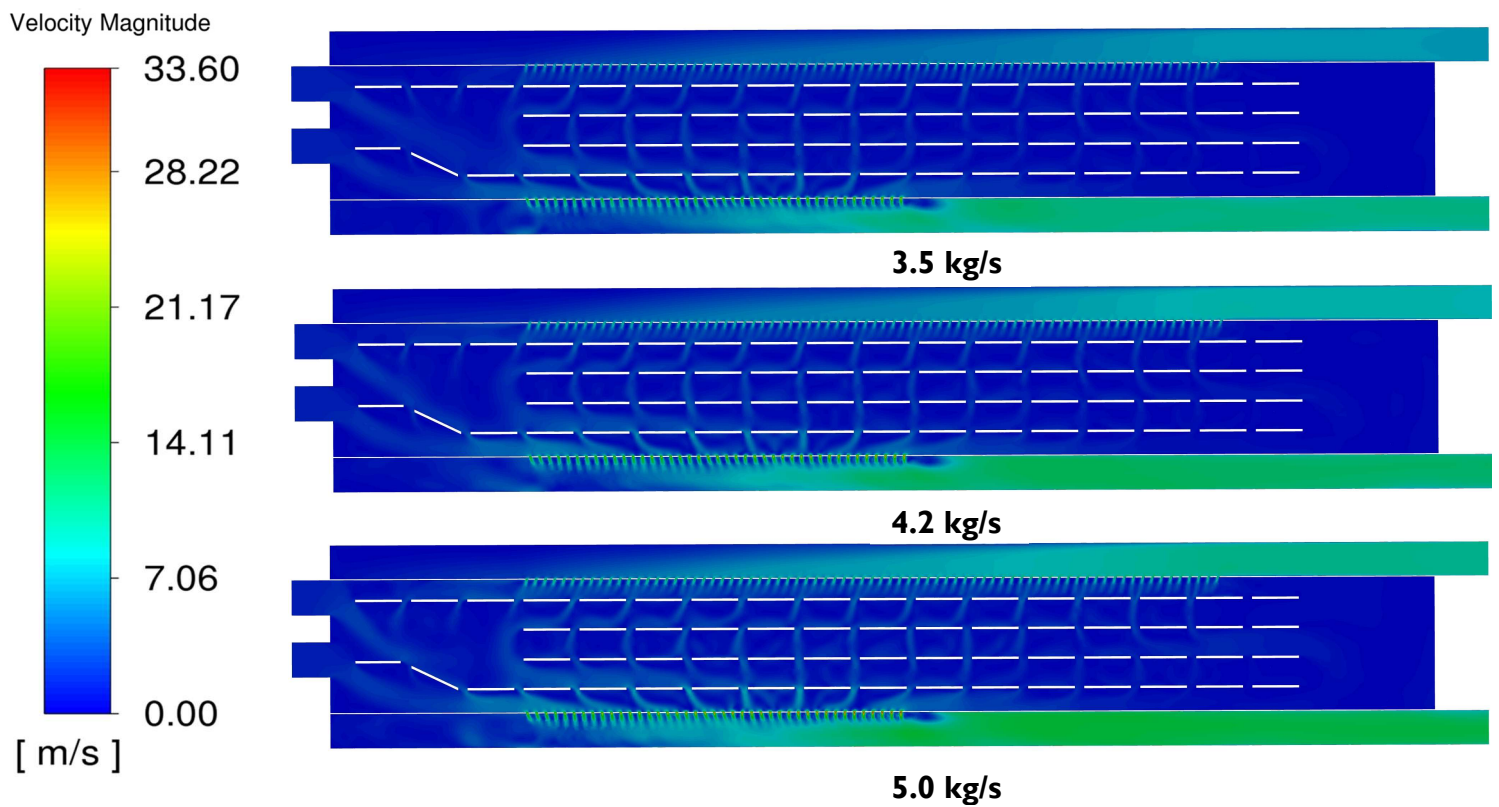


Figure 7: Contours of velocity

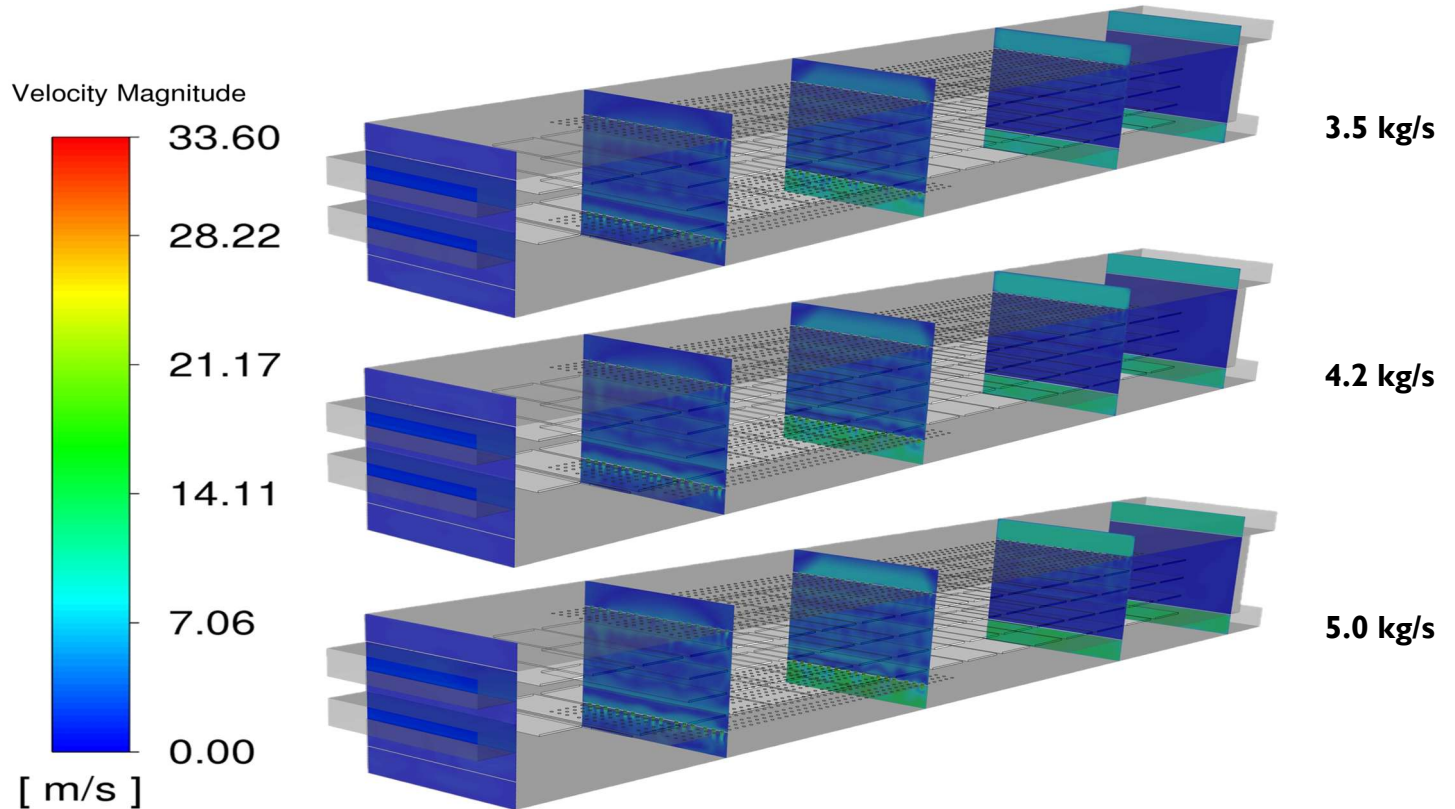


Figure 8: Contours of velocity at planes in z-direction

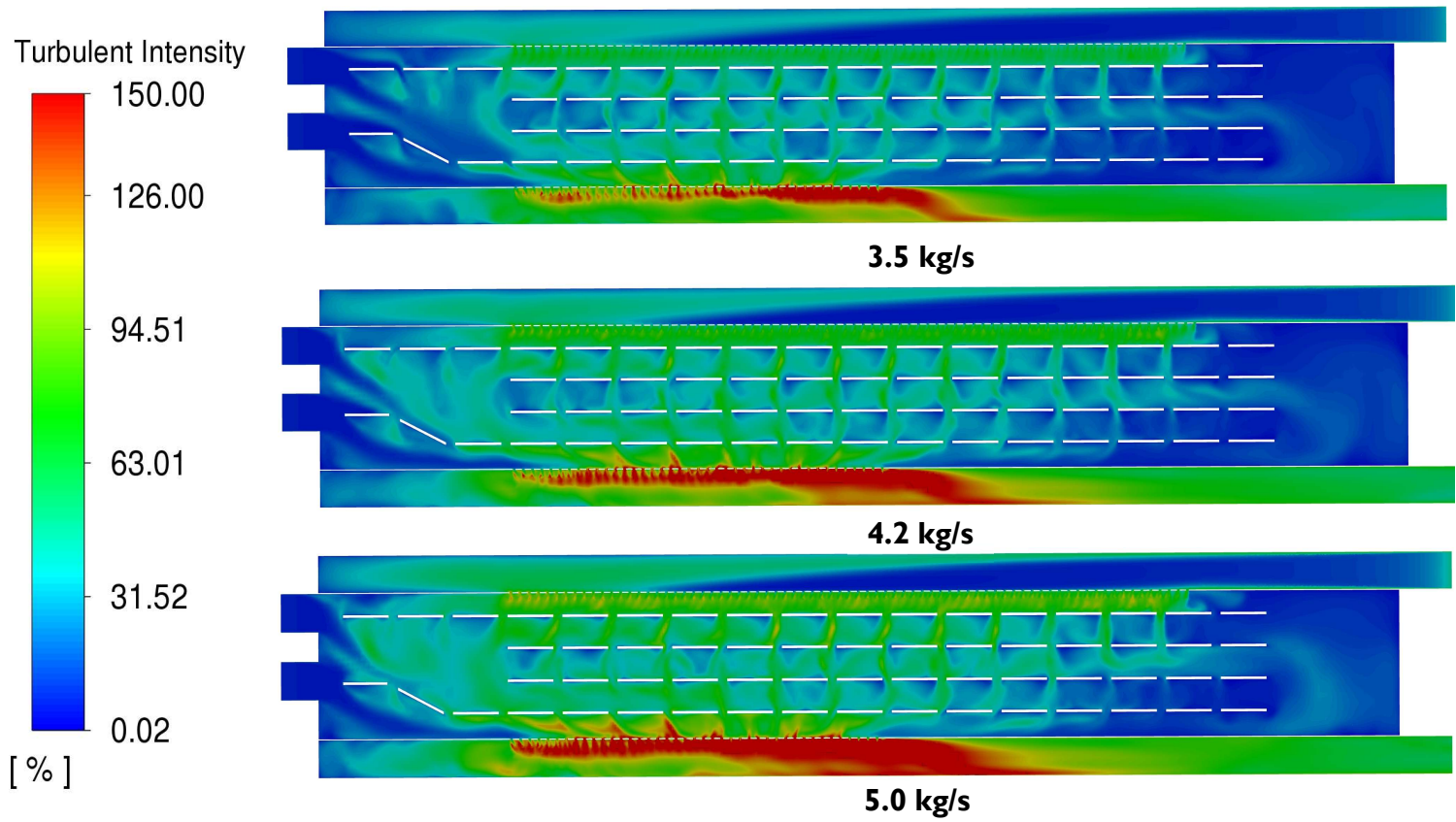


Figure 9: Contours of turbulent intensity

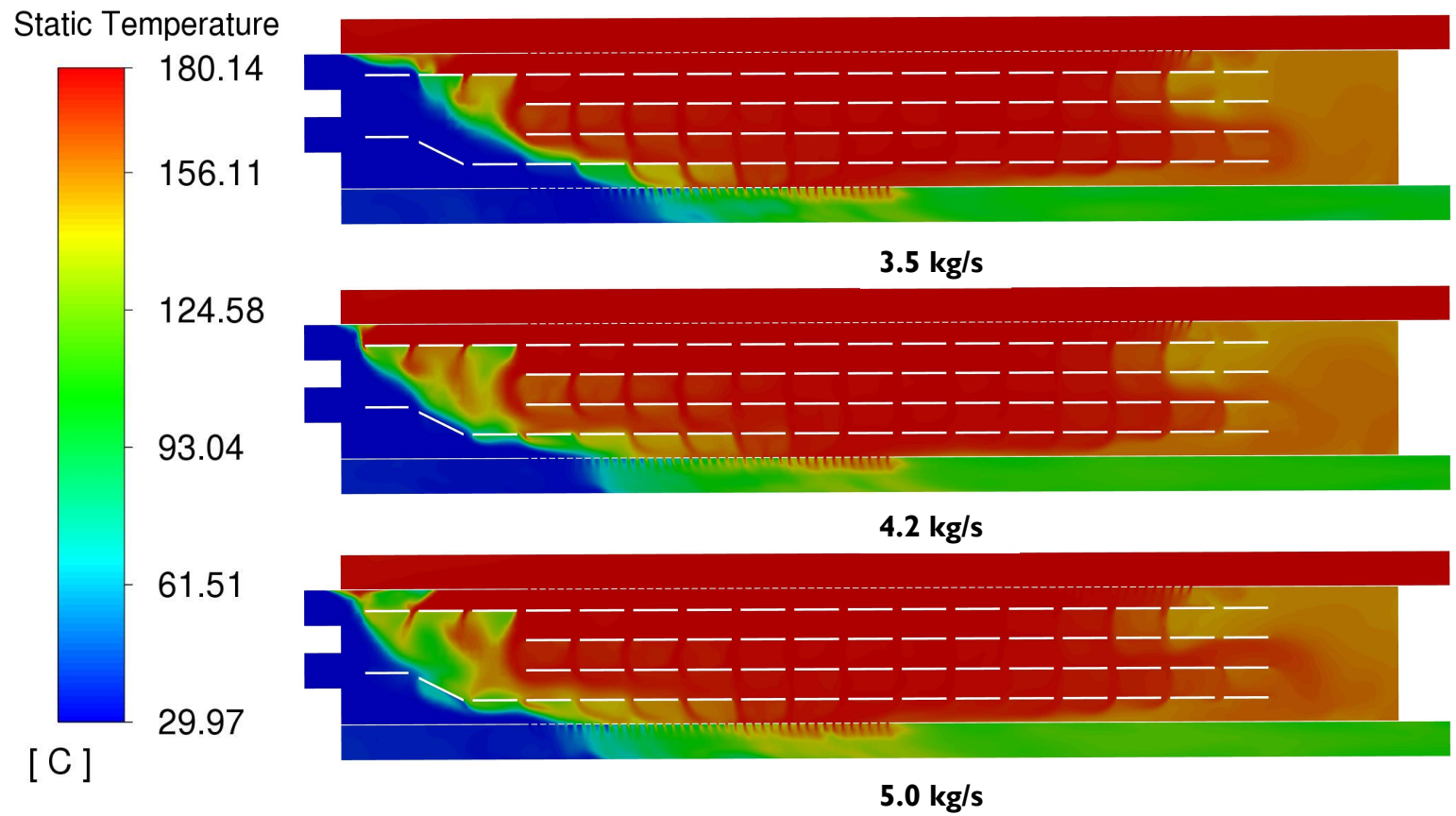


Figure 10: Contours of temperature

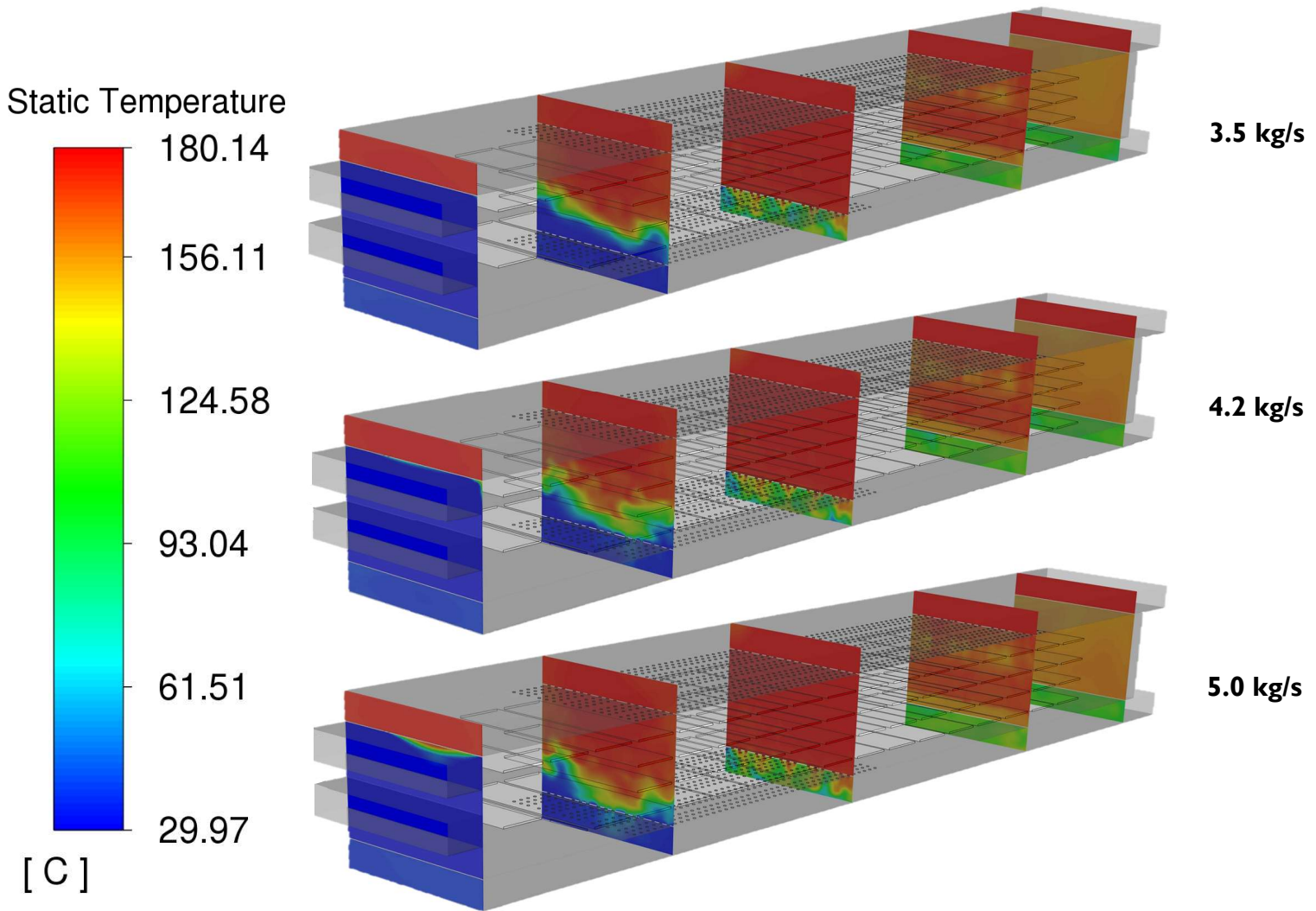


Figure 11: Contours of temperature at planes in z-direction

In all cases, the maximum velocity magnitude was observed in the lower holes. When the mass flow rate was 3.5 kg/s, the air coming from the exit section was observed to affect the direction of the air entering from the inlet section. However, at other mass flow rate values, its effect was minimal.

As the mass flow rate increases, a temperature increase is observed in the regions close to the exit. Therefore, if a significant increase is made in the mass flow rate value, the temperature value of the exit sections first at the top and then at the bottom will start to approach the inlet temperature. As the mass flow rate increases, it was observed that the local regions containing high temperatures inside the drying oven gradually become homogeneous.

6. DISCUSSIONS

In this study, three CFD simulations were performed on a drying oven with identical geometry, mesh, and boundary conditions, where the only variable was the inlet flow rate (3.5 kg/s, 4.2 kg/s, and 5.0 kg/s). The analysis focused on the flow pattern, temperature gradient, and velocity profiles, particularly around the top holes where the airflow directly impacts the paper pulp product.

6.1. Flow Pattern and Temperature Distribution

The simulations revealed that the overall flow pattern within the oven is largely independent of the inlet flow rate. In all cases, the cold room-temperature air enters the oven and predominantly exits through the bottom duct via the holes at the bottom. This behaviour indicates that the cold air is efficiently used as a fresh supply for the burner regardless of the flow rate. Additionally, the temperature distribution on the product surface remains uniform across the different cases. Since the inlet temperature is fixed at 180 °C for all analyses, the temperature gradient within the oven shows negligible variation with changes in flow rate. This consistency suggests that the system is robust in maintaining a steady thermal environment, which is crucial for the drying process.

6.2. Velocity Profiles and Implications for Product Integrity

While the flow pattern and temperature distribution remain similar across the different inlet flow rates, the velocity profiles, particularly near the top holes, show notable differences. These top holes are critical because the air exiting here directly impinges on the paper product. At higher velocities, there is a risk that the force of the air could disturb or damage the pulp, potentially causing it to fly out or become deformed.

The simulations indicate that:

- At an inlet flow rate of 5.0 kg/s, the velocity at the top holes ranges between 16 and 21 m/s.
- At 4.2 kg/s, the velocity is lower, ranging from 13 to 18 m/s.
- At the lowest flow rate of 3.5 kg/s, the velocity further decreases to between 10 and 14 m/s.

This trend clearly shows that increasing the inlet flow rate leads to higher air velocities at the top holes. Therefore, while higher flow rates might be beneficial for certain aspects of the drying process (e.g., potentially faster heat transfer), they also pose a risk to product integrity due to the higher impact forces. It is critical to balance these factors when designing and operating drying ovens, especially when working with delicate materials like paper pulp.

7. CONCLUSION

The CFD analysis demonstrates that although the flow pattern and temperature distribution within the drying oven are not significantly affected by the variation in inlet flow rates, the local velocity at the top holes increases with higher flow rates. This increase in velocity is a key parameter, as excessive air speeds can compromise the stability and quality of the paper product. Future work may involve optimizing the inlet flow rate or modifying the geometry of the top holes to mitigate the risk of product damage while maintaining efficient drying conditions. Additionally, in future works, detailed dynamic analysis can be performed by providing movement of the trays. Also, by adding real-size products onto the moving trays, the effects on the product can be analyzed. In this way, more realistic results can be obtained.

8. REFERENCES

1. D. Rehman & G.L. Morini (2020). Experimental validation of a two equation RANS transitional turbulence model for compressible microflow, University of Bologna.
2. Li, W., Ren, J., Hongde, J., & Ligrani, P. (2015). Assessment of six turbulence models for modeling and predicting narrow passage flows, part 1: Impingement jets. *Numerical Heat Transfer, Part A: Applications*, 69(2), 109–127.
3. P. A. Costa Rocha & H. H. Barbosa Rocha & F. O. Moura Carneiro & M. E. Vieira da Silva & C. Freitas de Andrade (2016). A case study on the calibration of the $k-\omega$ SST (shear stress transport) turbulence model for small scale wind turbines designed with cambered and symmetrical airfoils, *Energy*, Volume 97, 144-150.
4. Ganjare, A. V., & Patwardhan, A. W. (2019). CFD simulations of single-phase flow in settling tanks: comparison of turbulence models.
5. Zhai, Z. J., Zhang, Z., Zhang, W., & Chen, Q. Y. (2007). Evaluation of Various Turbulence Models in Predicting Airflow and Turbulence in Enclosed Environments by CFD: Part 1—Summary of Prevalent Turbulence Models. *HVAC&R Research*, 13(6), 853–870.
6. Zhang, Z., Zhang, W., Zhai, Z. J., & Chen, Q. Y. (2007). Evaluation of Various Turbulence Models in Predicting Airflow and Turbulence in Enclosed Environments by CFD: Part 2—Comparison with Experimental Data from Literature. *HVAC&R Research*, 871–886.
7. M.A. Abd Halim, N. A. R. Nik Mohd, M. N. Mohd Nasir & M. N. Dahalan (2018). The Evaluation of $k-\varepsilon$ and $k-\omega$ Turbulence Models in Modelling Flows and Performance of S-shaped Diffuser, Universiti Teknologi Malaysia
8. Sajad Mozaffari, Shang-Gui Cai, Jérôme Jacob & Pierre Sagaut (2024). Lattice Boltzmann $k-\omega$ SST based hybrid RANS/LES simulations of turbulent flows
9. Nieto, F., Hargreaves, D. M., Owen, J. S., & Hernández, S. (2015). On the applicability of 2D URANS and SST $k-\omega$ turbulence model to the fluid-structure interaction of rectangular cylinders. *Engineering Applications of Computational Fluid Mechanics*, 9(1), 157–173.
10. P. Mishra & K. R. Aharwal (2018). A review on selection of turbulence model for CFD analysis of air flow within a cold storage Materials Science and Engineering, Volume 402.
11. Zhu, L., Wang, T., Guo, Q., & Yuan, X. (2023). NN-augmented $k-\omega$ shear stress transport turbulence model for high-speed flows with shock-wave/boundary layer interaction. *Engineering Applications of Computational Fluid Mechanics*, 17(1).
12. Wallin S, Johansson AV. An explicit algebraic Reynolds stress model for incompressible and compressible turbulent flows. *Journal of Fluid Mechanics*. 2000; 403:89-132.

13. P.A. Costa Rocha, H.H. Barbosa Rocha, F.O. Moura Carneiro, M.E. Vieira da Silva & A. Valente Bueno (2014). *k*- ω SST (shear stress transport) turbulence model calibration: A case study on a small scale horizontal axis wind turbine.
14. T. R. K. Reddy, H. Kim, and J.-W. Park, “Renewable Biocomposite Properties and their Applications,” in InTech eBooks, 2016. doi: 10.5772/65475.
15. J. Song, R. Murphy, R. Narayan, and G. Davies, “Biodegradable and compostable alternatives to conventional plastics,” Jun. 15, 2009, Royal Society. doi: 10.1098/rstb.2008.0289.
16. Y. Ono, M. Hayashi, K. Yokoyama, T. Okamura, and N. Itsubo, “Environmental Assessment of Innovative Paper Recycling Technology Using Product Lifecycle Perspectives,” Feb. 29, 2020, Multidisciplinary Digital Publishing Institute. doi: 10.3390/resources9030023.
17. S. Tanthadiloke, W. Chankerd, A. Suwatthikul, P. Lipikanjanakul, I. M. Mujtaba, and P. Kittisupakorn, “3D computational fluid dynamics study of a drying process in a can making industry,” Aug. 06, 2016, Elsevier BV. doi: 10.1016/j.applthermaleng.2016.08.037.
18. A. Filios, D. P. Margaris, A.-G. Ghiaus, and D. Tzempelikos, "Industrial drying of wooden pallets - CFD analysis of air flow," ResearchGate, Oct. 2010. [Online]: <https://www.researchgate.net/publication/245542023>
19. Z. Khatir, A. R. Taherkhani, J. Paton, H. M. Thompson, N. Kapur, and V. Toropov, “Energy thermal management in commercial bread-baking using a multi-objective optimisation framework,” Jan. 23, 2015, Elsevier BV. doi: 10.1016/j.applthermaleng.2015.01.042
20. M. Pinelli and A. Suman, “Thermal and fluid dynamic analysis of an air-forced convection rotary bread-baking oven by means of an experimental and numerical approach,” Feb. 13, 2017, Elsevier BV. doi: 10.1016/j.applthermaleng.2017.02.037.
21. J. C. Z. Piaia, C. A. Claumann, M. B. Quadri, and A. Bolzan, “Air Flow CFD Modeling in an Industrial Convection Oven,” in Springer eBooks, Springer Nature, 2018, p. 1. doi: 10.1007/978-3-319-70945-1_1.
22. Tuncer Cebeci - *Analysis of Turbulent Flows with Computer Programs*. Butterworth-Heinemann (2013)
23. Yunus A. Cengel & John M. Cimbala. *Fluid Mechanics: Fundamentals And Applications*. New York, McGraw-Hill (2014).

24. Hermann Schlichting (Deceased), Klaus Gersten. *Boundary-Layer Theory*. Berlin-Heidelberg Springer (2017).